



OPEN

## Spontaneously formed gradient chemical compositional structures of niobium doped titanium dioxide nanoparticles enhance ultraviolet- and visible-light photocatalytic performance

Naoki Tarutani<sup>1,2,3✉</sup>, Ryuma Kato<sup>2</sup>, Tetsuo Uchikoshi<sup>3,4</sup> & Takamasa Ishigaki<sup>2,3✉</sup>

Semiconductor photocatalysts showing excellent performance under irradiation of both ultraviolet (UV)- and visible (VIS)-light are highly demanded towards realization of sustainable energy systems. TiO<sub>2</sub> is one of the most common photocatalysts and has been widely investigated as candidate showing UV/VIS responsive performance. In this study, we report synthesis of Nb doped TiO<sub>2</sub> by environmentally benign mechanochemical reaction. Nb atoms were successfully incorporated into TiO<sub>2</sub> lattice by applying mechanical energy. As synthesized Nb doped TiO<sub>2</sub> were metastable phase and formed chemical compositional gradient structure of poorly Nb doped TiO<sub>2</sub> core and highly Nb doped TiO<sub>2</sub> surface after high temperature heat treatment. It was found that formed gradient chemical compositional heterojunctions effectively enhanced photocatalytic performance of Nb doped TiO<sub>2</sub> under both of UV- and VIS-light irradiation, which is different trend compared with Nb doped TiO<sub>2</sub> prepared through conventional methods. The approach shown here will be employed for versatile systems because of simple and environmentally benign process.

In the last decade, there is a numerous number of studies about functionality improvement of semiconductor photocatalysts to achieve both of ultraviolet (UV)-light and visible (VIS)-light responsive performance. Several strategies, such as band gap engineering by doping cations and/or anions, modification of surface structures, and design heterojunction with cocatalysts of metals or semiconductors, were employed to achieve UV/VIS responsive photocatalytic performance<sup>1-4</sup>. Although typical methods, such as solid state reaction<sup>5,6</sup>, solvothermal/hydrothermal reaction<sup>7-10</sup>, and vacuum deposition<sup>11,12</sup>, are successful approach to synthesize doped semiconductors and heterojunction materials, it is necessary to employ energy consuming and/or high environmental burden conditions, such as quite high temperature sintering, toxic gas flow, high pressure, and vacuum condition, which will give negative impact on environment. Mechanochemical process is known as a facile and an environmentally benign method<sup>13,14</sup>. Mechanochemical reaction often produces unique metastable materials which cannot be prepared by conventional thermochemical techniques<sup>15</sup>. For example, metastable amorphous calcium carbonate phase was successfully stabilized by mechanochemical Na doping<sup>16</sup>. Synthesis of metastable Li<sub>2</sub>OHCl is another example, which showed higher ionic conductivity compared with thermodynamically stable phase<sup>17</sup>. Nowadays, mechanochemical process is widely employed to synthesize not only typical organic and inorganic compounds, but also doped compounds and composites<sup>18-21</sup>. Moreover, the mechanisms of the co-crystallization and metastable formation through mechanochemical reactions were reported in the specific systems<sup>22,23</sup>. There

<sup>1</sup>Applied Chemistry Program, Graduate School of Advanced Science and Engineering, Hiroshima University, 1-4-1 Kagamiyama, Higashi-Hiroshima, Hiroshima 739-8527, Japan. <sup>2</sup>Department of Chemical Science and Technology, Faculty of Bioscience and Applied Chemistry, Hosei University, 3-7-2 Kajino-cho, Koganei, Tokyo 184-8584, Japan. <sup>3</sup>Research Center for Micro-Nano Technology, Hosei University, 3-11-15 Midori-cho, Koganei, Tokyo 184-0003, Japan. <sup>4</sup>Research Center for Functional Materials, National Institute for Materials Science, 1-2-1, Sengen, Tsukuba 305-0047, Japan. ✉email: n-tarutani@hiroshima-u.ac.jp; ishigaki@hosei.ac.jp

is a strong demand to develop facile and promising process by using mechanochemical reaction for highly functional materials, such as UV- and VIS-light responsive semiconductor photocatalysts.

Titanium dioxide, TiO<sub>2</sub>, is one of the most investigated semiconductor which shows excellent photocatalytic activity under irradiation of UV-light<sup>24</sup>. Doping of metals/nonmetals and/or formation of heterojunction of TiO<sub>2</sub>/semiconductors were reported to effectively enhance photocatalytic performance<sup>25,26</sup>. For a preparation of doped TiO<sub>2</sub> through mechanochemical reaction, metals and metal salts were used as dopant sources of cations in general. However, metals tend to weld each other to form composite rather than doping and metal salts gave unexpected doping from counter anions<sup>18,27</sup>. To avoid these drawbacks, it is necessary to optimize numerous mechanochemical reaction parameters, such as gas atmosphere, milling media, milling speed, milling time, and ball-to-powder weight ratio. Use of metal oxides instead of metals and metal salts is expected to be easier and successful way to dope metal cations into TiO<sub>2</sub> matrices.

In this study, we focused on the fabrication of Nb doped TiO<sub>2</sub> by using mechanochemical process. Commercially available TiO<sub>2</sub> nanoparticles (mixture of anatase and rutile phase) was employed as a starting material and synthesized TiNb<sub>2</sub>O<sub>7</sub> microparticles was used as a Nb doping agent. Variety amounts of Nb atom were homogeneously incorporated into both of anatase and rutile nanoparticles by wet mechanochemical process. Nb doped anatase nanoparticles showed improved thermal stability owing to the pinning Nb atoms. It was found that heat treatment led Nb atoms distributed inhomogeneously at surface of nanoparticles to form gradient chemical compositional structures of poorly Nb doped TiO<sub>2</sub> and highly Nb doped TiO<sub>2</sub>. The Nb doped TiO<sub>2</sub> with chemical compositional gradient structure showed enhanced photocatalytic activity under both of UV- and VIS-light irradiation. Although Nb doped TiO<sub>2</sub> were synthesized through various methods, such as pulsed laser deposition<sup>28,29</sup>, sol-gel technique<sup>30,31</sup>, thermal plasma processing<sup>32</sup>, and spray pyrolysis<sup>33</sup>, chemical compositional gradient structures have not been reported. This indicates that mechanochemically synthesized materials are key to form the gradient structure and enhance photocatalytic property. The method reported here is a simple and facile approach, hence it is expected to widely apply other dopant-semiconductor systems towards highly functionalized photocatalysts.

## Methods

**Chemicals.** Titanium(IV) tetraisopropoxide (TTIP, 95%), niobium(V) pentaethoxide (NPE, 99.9%), diethanolamine (99%), polyethyleneimine ( $M_w = 1800$ ), methyl orange (MO), sodium dihydrogen phosphate (NaH<sub>2</sub>PO<sub>4</sub>, 85%), phosphoric acid (H<sub>3</sub>PO<sub>4</sub>, 85%), ethanol (99.5%) were used as received. H<sub>3</sub>PO<sub>4</sub> was purchased from Kanto Chemical Holdings. All other reagents were purchased from Wako Pure Chemicals Industries, Ltd. Ultrapure water of 18.2 MΩ-cm resistivity was used in all experiments.

**Synthesis of TiNb<sub>2</sub>O<sub>7</sub> microparticles.** TTIP (1 mmol), NPE (2 mmol), and diethanolamine (2 mmol) were dissolved in 5 mL of ethanol. After stirring for 20 min, homogenous sol was obtained. Water (35 mmol) was added to the sol under vigorous stirring and keep stirring at least for 5 min to obtain gel. Gelatinous precipitates were dried at 100 °C for 12 h. Dried powders were heat treated at 1150 °C for 3 h (ramp rate: 5 °C/min). Heat treated powder of TiNb<sub>2</sub>O<sub>7</sub> was employed as a Nb source in subsequent mechanochemical process because TiNb<sub>2</sub>O<sub>7</sub> was reportedly segregated from Nb doped TiO<sub>2</sub> only after high temperature heat treatment that means TiNb<sub>2</sub>O<sub>7</sub> will be highly compatible with TiO<sub>2</sub><sup>32</sup>.

**Mechanochemical synthesis of Nb-doped TiO<sub>2</sub> nanoparticles.** Obtained TiNb<sub>2</sub>O<sub>7</sub> powders were mixed with commercial anatase-rutile TiO<sub>2</sub> nanoparticles (EVONIK AEROXIDE® P25, Nippon Aerosil, Tokyo, Japan) with a molar ratio of Nb/(Ti + Nb) = 0 (without TiNb<sub>2</sub>O<sub>7</sub>), 0.02, 0.05, and 0.10. After grounded for 30 min in a mortar, mixed powders (2.5 g) were dispersed in 20 mL of ethanol solution including polyethyleneimine ( $7.2 \times 10^{-2}$  mmol). Obtained suspensions were sealed in zirconia pod (inner volume of 80 mL) and milled in a tilted rotation planetary ball mill (Planet M2-3F, Nagao System Inc.) at revolution speed of 700 rpm and rotation speed of 1750 rpm (152 G) for 2 h with zirconia balls (5 mm in diameter, #243, 83.5 g). Milled suspensions were dried at room temperature for 5 days and heat treated at 500–900 °C for 3 h (ramp rate: 5 °C/min, cooling rate: 2 °C/min). The powders prepared through this process were denoted as NTO-*x*-*y*, where *x* and *y* are nominal Nb/(Ti + Nb) in percentage ( $0 \leq x \leq 10$ ) and heat treatment temperature ( $500 \leq y \leq 900$ ) (As dried samples before heat treatment are denoted as NTO-*x*-dry).

**Photocatalytic test.** The solution pH was kept at 2.1 using buffer solution to avoid agglomeration of nanoparticles during photocatalytic test, which changes background light scattering by particles. Phosphate buffer solution (0.10 mol/L, pH = 2.1) were prepared using NaH<sub>2</sub>PO<sub>4</sub> and H<sub>3</sub>PO<sub>4</sub>. Sample powders (10 mg) were dispersed in 6 mL of buffered aqueous solution and ultrasonicated for 30 min. MO buffered aqueous solution (20 μmol/L, 20 μL) was added to the suspensions. Colored suspensions (3 mL) in close capped quartz cell (1 × 1 cm<sup>2</sup> base rectangular cell) were exposed to UV/VIS-light after stirring in dark condition. UV light and VIS light were generated by UVF-203S Type-A light source (San-Ei Electric Co., Ltd., Japan) (365 nm) and UVF-203S Type-C light source (San-Ei Electric Co., Ltd., Japan) (405 and 436 nm) with intensities of 60 and 255 mW/cm<sup>2</sup>, respectively. The light probes were contacted to the quartz cell, which means the light-to-solution distance was same for all the experiments, ~ 1 mm. After appropriate irradiation time, the suspensions were left for 30 s without stirring and set in a UV-vis spectroscopy to determine MO concentration from the  $F(R_{\infty})$  at 514 nm of diffuse reflectance spectra using calibration curve.

**Characterization.** A field emission scanning microscope (SEM; S-8020, Hitachi High-Technologies Corp., Japan) equipped with energy dispersed X-ray spectroscopy (EDS) was used for evaluation of particle size and

elemental composition. A transmission electron microscope (TEM; JEM-2100F, JEOL Ltd., Japan) equipped with EDS and scanning TEM mode (STEM) was employed at an operating voltage of 200 kV to clarify the crystal phase and elemental composition of individual particles. Powder X-ray diffraction (XRD) (SmartLab, Rigaku Corp., Japan) using Cu K $\alpha$  radiation ( $\lambda = 0.1544$  nm) equipped with one dimensional detector was used to characterize crystal phases of samples. X-ray photoelectron spectrometer (XPS) analyses were carried out with ESCA-5600 (Ulvac-Phi, Japan) using a monochromatic Al K $\alpha$  source (1486.6 eV, 200 W) to evaluate an elemental composition of adjacent surface of particles and an oxidation state of Ti and Nb atoms. The instrument work function was calibrated to give an Au 4f $_{7/2}$  of metallic gold binding energy of 83.95 eV  $\pm$  0.1 eV. Survey spectra and high-resolution spectra were collected with a step of 0.4 and 0.05 eV, respectively. The obtained spectra were calibrated using C 1s binding energy (284.8 eV) of the samples as an internal standard. Ultraviolet-visible (UV-Vis) spectroscopy (V-650 spectrophotometer, JASCO Corp., Japan) equipped with an integrating sphere was used to characterize optical band gap of samples and evaluation of decolorization of MO solution. The reflectance values of obtained diffuse reflectance spectra were transformed to Kubelka–Munk units,  $F(R_{\infty})$  by using Eq. (1)

$$F(R_{\infty}) = (1 - F(R_{\infty,s}))^2 / 2(F(R_{\infty,s})) \quad (1)$$

where  $F(R_{\infty,s})$  is measured reflectance value. Raman spectroscopy (RAMANtouch, Nanophoton Corp., Japan) was employed to characterize crystal phases and defects (excitation: 532 nm). The N $_2$  adsorption–desorption measurement using Belsorp-18 (Bel Japan Inc., Japan) was employed to evaluate specific surface area by the Brunauer–Emmett–Teller (BET) method.

## Results and discussion

**Incorporation of Nb into TiO $_2$  nanoparticles through mechanochemical treatment.** TTIP and NPE were used as precursors to synthesize TiNb $_2$ O $_7$  as a Nb doping agent. Addition of water to ethanolic solution, including TTIP, NPE, and diethanolamine, triggered hydrolysis and condensation of both metal alkoxides. During reaction, diethanolamine worked as a reaction controlling agent, which hinder vigorous reaction of NPE and enabled to form homogenous Ti and Nb mixed precipitates. Dried precipitates were characterized as poorly crystalline TiNb $_2$ O $_7$  by XRD measurement (Figure S1). The precipitates were heat treated at 1150 °C for 3 h. Heat treated precipitates were characterized as well-crystalline TiNb $_2$ O $_7$  with a crystallite size of 63.7 nm calculated using 110 diffraction peak. Obtained TiNb $_2$ O $_7$  showed angulate shape with a particle size of 840  $\pm$  359 nm (Fig. 1a,d). TiNb $_2$ O $_7$  microparticles and commercially available TiO $_2$  nanoparticles (particle diameter of 44.1  $\pm$  16.7 nm) (Fig. 1b,e) were mixed and mechanochemically treated. After mechanochemical treatment, as dried powder (NTO-5-dry, see experimental section for sample IDs) showed the particle size of 43.8  $\pm$  20.0 nm which is comparable size to the pristine TiO $_2$  (Fig. 1c,f). Figure 2a,b are TEM image of NTO-5-dry. The lattice fringe close to particle surface became disorder after mechanochemical treatment, which is a feature of amorphous phase. Raman spectra of pristine TiO $_2$ , NTO-5-dry, and NTO-5-600 were shown in Figure S2. The peak around 145 cm $^{-1}$ , assigned as E $_g$  mode of symmetric stretching vibrations of O–Ti–O bonds of anatase phase<sup>34</sup>, was shifted to 148 cm $^{-1}$  after mechanochemical treatment (NTO-5-dry), which indicates formation of oxygen vacancies<sup>13</sup>. Grayish color of NTO-5-dry powder agrees formation of oxygen vacancies in TiO $_2$  matrix<sup>35</sup>. The peak shifted back to 145 cm $^{-1}$  after heat treatment at 600 °C indicating elimination of vacancies. The atomic ratios of Nb/(Ti + Nb) evaluated by SEM–EDS and XPS were well matched with nominal molar ratio (Table S1). Figure 2c shows the local Nb/(Ti + Nb) ratio measured by STEM–EDS line scanning. The scanned line was shown in Fig. 2a as green dots, which crosses both of rutile and anatase nanoparticles. Nb atoms were detected at entire points, which implies that Nb atoms were homogeneously incorporated in both of anatase and rutile nanoparticles.

XRD patterns of powders before and after mechanochemical treatment were shown in Fig. 2d with the pattern of TiNb $_2$ O $_7$  microparticles. Detected crystalline species were anatase and rutile phase with trace amount of TiNb $_2$ O $_7$  after mechanochemical reaction. Crystallite size of TiNb $_2$ O $_7$ , anatase, and rutile before/after mechanochemical treatment were calculated as 63.7/31.7 nm, 21.4/20.7 nm, and 29.2/25.8 nm, respectively. Drastic crystallite size reduction of TiNb $_2$ O $_7$  indicates that TiO $_2$  crystals were more stable than TiNb $_2$ O $_7$  crystals against mechanical energy. Reported Young's modulus of each crystals (255.5–311.6 GPa for TiO $_2$ <sup>36</sup> and 173  $\pm$  5 GPa for TiNb $_2$ O $_7$ <sup>37</sup>) supports that preferential amorphization of TiNb $_2$ O $_7$  crystals took place during mechanochemical treatment. Lattice volume of anatase (135.98(8) Å $^3$ ) and rutile (62.48(3) Å $^3$ ) phases of NTO-5-dry was comparable to those of pristine TiO $_2$  (136.01(7) Å $^3$  and 62.51(3) Å $^3$ ). This may be result of competitive effects between lattice expansion due to Nb substitution<sup>31,32</sup> and lattice contraction due to interstitial oxygen in TiO $_2$ <sup>38</sup> incorporated to compensate charge balance<sup>39,40</sup>.

Figure 3a shows XRD patterns of powders heat treated at 500–900 °C (NTO-5- $y$ ,  $y = 500$ –900). The intensity of peaks assigned as rutile phase increased with increasing the heat treatment temperature. The weight fraction of rutile phase against anatase phase,  $f_R$ , was calculated using following Eq. (2)<sup>41</sup>;

$$f_R = 1 / (1 + 0.79 \cdot I_A / I_R) \quad (2)$$

where  $I_A$  and  $I_R$  are integrated intensities of rutile 110 diffraction peak and anatase 101 diffraction peak, respectively. Temperature dependent changes of  $f_R$  were shown in Fig. 3b. NTO-0-dry and NTO-5-dry showed  $f_R$  comparable to pristine TiO $_2$ . Although a phase transition from anatase to rutile by mechanochemical treatment was reported<sup>42</sup>, amorphous layer formation on the surface of nanoparticles and preferential amorphization of TiNb $_2$ O $_7$  may consume mechanical energy and retard phase transition of anatase. In the case of ground mixed powders of pristine TiO $_2$  and TiNb $_2$ O $_7$  in a mortar,  $f_R$  drastically increased with temperature and reached  $f_R \sim 1.0$

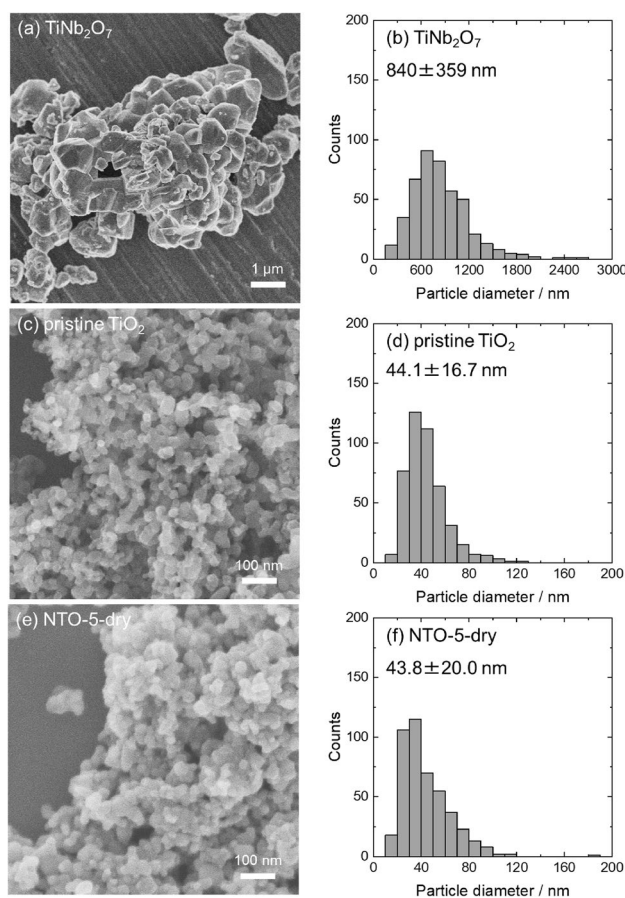


**Figure 1.** (a), (c), (e) SEM images and (b), (d), (f) corresponding particle diameter distributions (statistics of 450 particles) of synthesized  $\text{TiNb}_2\text{O}_7$  microparticles, pristine  $\text{TiO}_2$  nanoparticles, and NTO-5-dry.

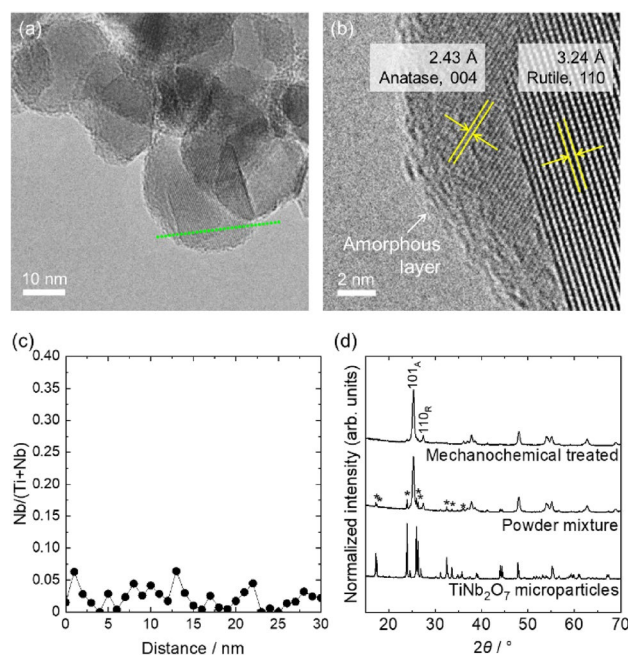


**Figure 2.** (a,b) TEM images and (c) Nb/(Ti + Nb) calculated from STEM-EDS line scan of NTO-5-dry. Green dots in (a) are scanned points of STEM-EDS shown in (c). (d) XRD patterns of  $\text{TiNb}_2\text{O}_7$  microparticles, powder mixture of pristine  $\text{TiO}_2$  and  $\text{TiNb}_2\text{O}_7$  and mechanochemical treated powder (nominal Nb/(Ti + Nb) = 0.05). \*  $\text{TiNb}_2\text{O}_7$ ; JCPDS #00-072-0116.

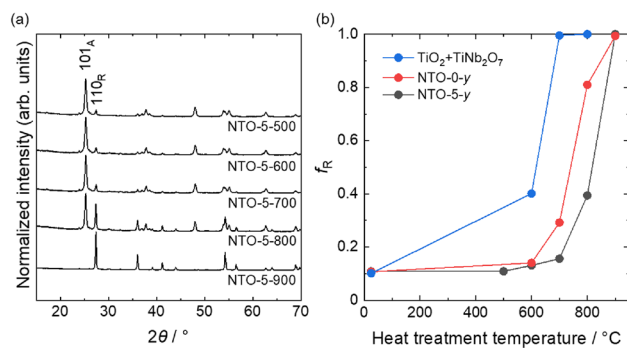


**Figure 3.** (a) XRD patterns of NTO-5- $y$  ( $y=500-900$ ).  $101_A$  and  $110_R$  correspond to 101 diffraction peak of anatase and 110 diffraction peak of rutile, respectively. (b) Rutile phase weight fraction,  $f_R$ , against anatase phase calculated from corresponding XRD patterns. As mixed pristine  $\text{TiO}_2$  and  $\text{TiNb}_2\text{O}_7$ , NTO-0-dry, and NTO-5-dry are plotted at temperature of 25 °C.

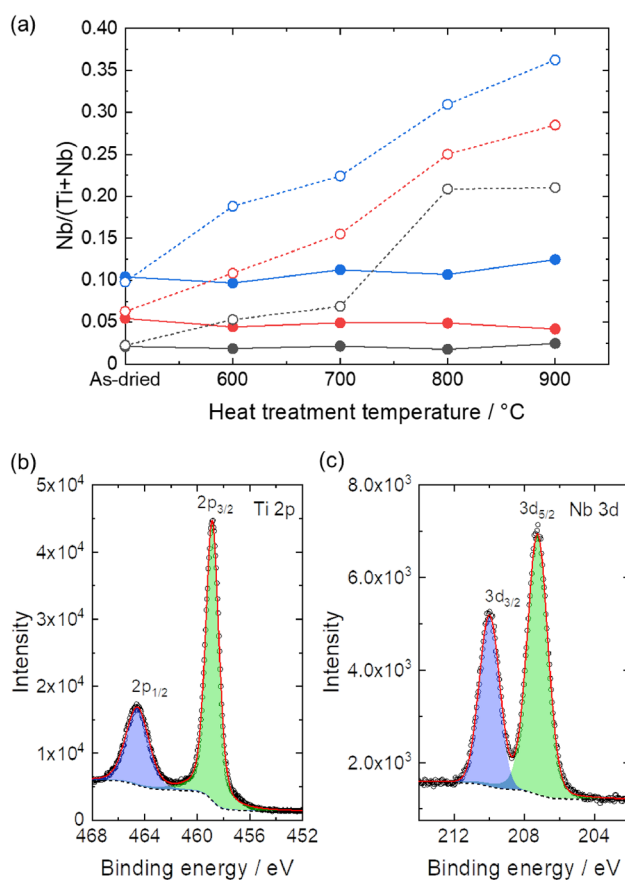


**Figure 4.** (a) Nb/(Ti+ Nb) values calculated from SEM-EDS (filled symbol with solid lines) and XPS (open symbol with dot lines) spectra of NTO-2- $y$  (black), NTO-5- $y$  (red) and NTO-10- $y$  (blue). (b) Ti 2p and (c) Nb 3d XPS spectra of NTO-5-600 (open circles, black dot line, blue/green area, and red solid line denote experimental data, background, fitted curves, and cumulative curves of fitted curves).

after heat treatment at 700 °C. NTO-0- $y$  showed smaller  $f_R$  than powder mixtures at each heat treatment temperature, which indicates formed surface amorphous layer worked as effective grain boundary and retarded phase transition. In the case of NTO-5- $y$ , ~60% of anatase crystals were remained even after heat treated at 800 °C. In addition to amorphous layer formation, incorporated Nb atoms worked as pinning sites and improved thermal stability<sup>31,32</sup>. Thermal stability of anatase phase was also improved in the case of NTO-2- $y$  and NTO-10- $y$  (Figure S3a), which indicates that incorporated Nb atoms effectively worked as pinning sites even if small quantity.

Chemical compositions of heat-treated powders were investigated by using SEM-EDS and XPS techniques (Fig. 4a). Nb/(Ti+ Nb) ratio calculated from SEM-EDS spectra of NTO-2- $y$ , NTO-5- $y$ , and NTO-10- $y$  were well matched with nominal value. On the other hand, Nb/(Ti+ Nb) ratio calculated using XPS spectra were

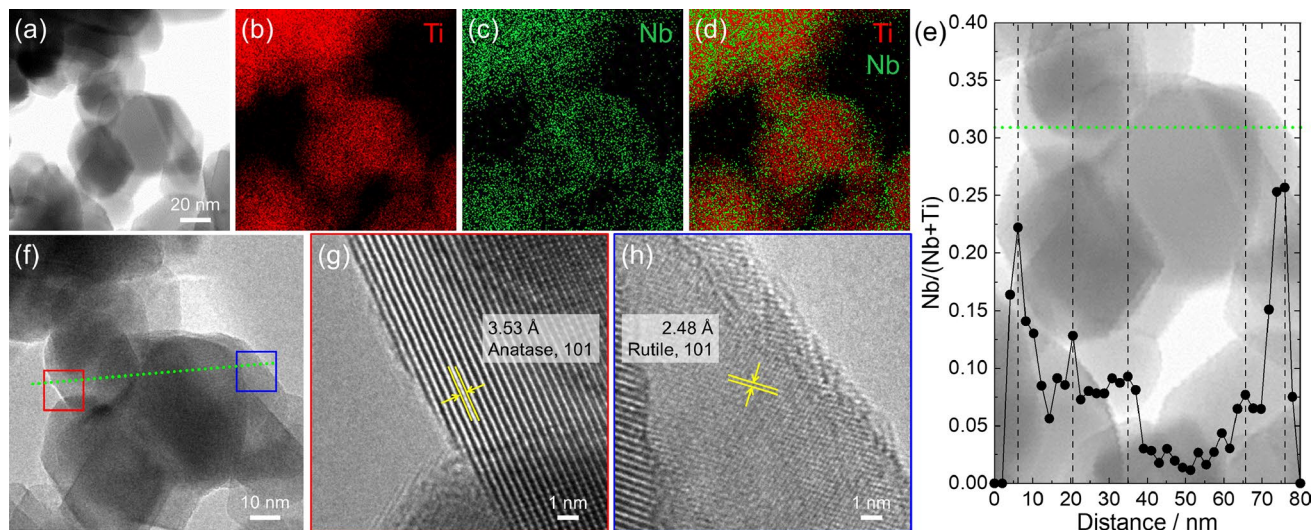


**Figure 5.** (a) STEM image, (b)–(d) STEM-EDS mapping images, and (e) STEM-EDS line scanned profile of NTO-5-800. The dot line in (e) represents the scan points at the edge of the particles. (f)–(h) TEM images of NTO-5-800. In (f), red and blue squares are magnified area of (g) and (h) and green dots are STEM-EDS line scanned points shown in (e).

increased with increasing the heat treatment temperature, which means that heat treated Nb doped  $\text{TiO}_2$  have inhomogeneous chemical composition between surface and core of the particles. The Nb/(Ti + Nb) increased with increasing heat treatment temperature independently of the integrated area of diffraction peak of  $\text{TiNb}_2\text{O}_7$ , except NTO-10-900 (Figure S3b). This implies that Nb atoms were still incorporated in the  $\text{TiO}_2$  lattice and/or in amorphous like Nb-rich oxide phases at the surface of nanoparticles. Figure 4b,c were XPS Ti 2p and Nb 3d core level spectrum of NTO-5-600. Both spectra were fitted with two of peak functions. The fitted peak positions of Ti  $2p_{1/2}$  and Ti  $2p_{3/2}$  were 464.6 eV and 458.9 eV, respectively, which is a good agreement with reported value of  $\text{Ti}^{4+}$ <sup>43</sup>. The fitted peak positions of Nb  $3d_{3/2}$  and Nb  $3d_{5/2}$  were 210.0 eV and 207.2 eV, respectively. The Nb  $3d_{5/2}$  peak position is intermediate of  $\text{Nb}^{4+}$  (205.9 eV) and  $\text{Nb}^{5+}$  (207.5 eV)<sup>44</sup>. In the case of titanium niobium oxides family ( $\text{TiNb}_m\text{O}_{2+2.5m}$ ), relatively Ti rich compounds, such as  $\text{TiNb}_2\text{O}_7$  ( $m=2$ )<sup>45</sup> and  $\text{Ti}_2\text{Nb}_{10}\text{O}_{29}$  ( $m=5$ )<sup>46</sup> showed Nb  $3d_{5/2}$  peak position same as mixture of  $\text{Nb}^{4+}$  and  $\text{Nb}^{5+}$  in Nb-doped  $\text{TiO}_2$ <sup>31</sup> and relatively Nb rich compounds, such as  $\text{TiNb}_6\text{O}_{17}$  ( $m=6$ )<sup>47</sup> and  $\text{TiNb}_{24}\text{O}_{62}$  ( $m=24$ )<sup>48</sup> showed the peak position same as  $\text{Nb}^{5+}$  in  $\text{Nb}_2\text{O}_5$ . Considering Nb/(Ti + Nb) of NTO-5-600 was 0.11, it is reliable that Nb was exist as a mixture of  $\text{Nb}^{4+}$  and  $\text{Nb}^{5+}$ . All the samples showed Ti  $2p_{3/2}$  = 458.8 ± 0.2 eV and Nb  $3d_{5/2}$  = 207.1 ± 0.2 eV which indicate that the oxidation states of Ti and Nb were stable during heat treatment.

Further analysis was demonstrated using TEM and STEM-EDS. Figure 5a–d were STEM and STEM-EDS mapping images. Although Ti atoms were homogeneously distributed in the individual particles, Nb atoms inhomogeneously distributed around the edges of the particles. Figure 5e is the result of line scanned STEM-EDS analysis. Nb/(Ti + Nb) clearly increased at the scan point of the particle edges. Figure 5f–h are TEM image of the location where STEM-EDS mapping and line scan were taken. The start and end points of STEM-EDS line scan were located at the nanoparticles of anatase and rutile, respectively. Therefore, Nb rich  $\text{TiO}_2$  (Nb/(Ti + Nb) ~ 0.25) were formed at the surface of both anatase and rutile nanoparticles. The changes of lattice fringes were analysed by fast Fourier transform method (Figure S4). Clear spots corresponding to anatase 101 and rutile 101 lattice fringes were obtained at the analysis area enough distant from the particle surface. On the other hand, the fast Fourier transform images prepared using the analysis area around surface showed blurred spots with broad ring patterns, which indicates segregation of Nb atoms at the surface made the lattice disordered. XPS, STEM-EDS, and TEM analyses indicate that gradient chemical composition was spontaneously developed; poorly Nb doped  $\text{TiO}_2$  at the core of the nanoparticles and highly Nb doped  $\text{TiO}_2$  at the surface of nanoparticles.

Optical properties were investigated using UV–Vis diffuse reflectance spectroscopy (Figure S5 and S6). Obtained diffuse reflectance spectra were converted to  $(F(R_\infty)h\nu)^2$  versus  $h\nu$  and  $(F(R_\infty)h\nu)^{1/2}$  versus  $h\nu$  plots for an evaluation of direct and indirect transitions, respectively. Direct band gap energies were decreased with increasing heat treatment temperature (Figure S6a). On the other hands, indirect band gap energies were slightly increased with increasing heat treatment temperature (Figure S6b). There is a rough linear relationship between  $f_R$  and the direct band gap energy (Figure S6c) and between Nb/(Ti + Nb) and indirect band gap energy (Figure S6d). These results indicate that rutile phase and niobium titanium oxide phases are dominant factor of direct and indirect band gaps, respectively. In fact, direct and indirect band gaps were approaching to corresponding band gaps; direct band gap of rutile phase is 3.0 eV<sup>49</sup> and indirect band gap of  $\text{TiNb}_2\text{O}_7$  phase is 3.1 eV<sup>45</sup>, respectively.

In summary, mechanochemical treatment using  $\text{TiO}_2$  nanoparticles and  $\text{TiNb}_2\text{O}_7$  microparticles produced Nb doped  $\text{TiO}_2$  nanoparticles as a result of preferential amorphization of  $\text{TiNb}_2\text{O}_7$  phase. Homogeneously incorporated Nb atoms diffused to the surface of nanoparticles after heat treatment. Resultant nanoparticles of both

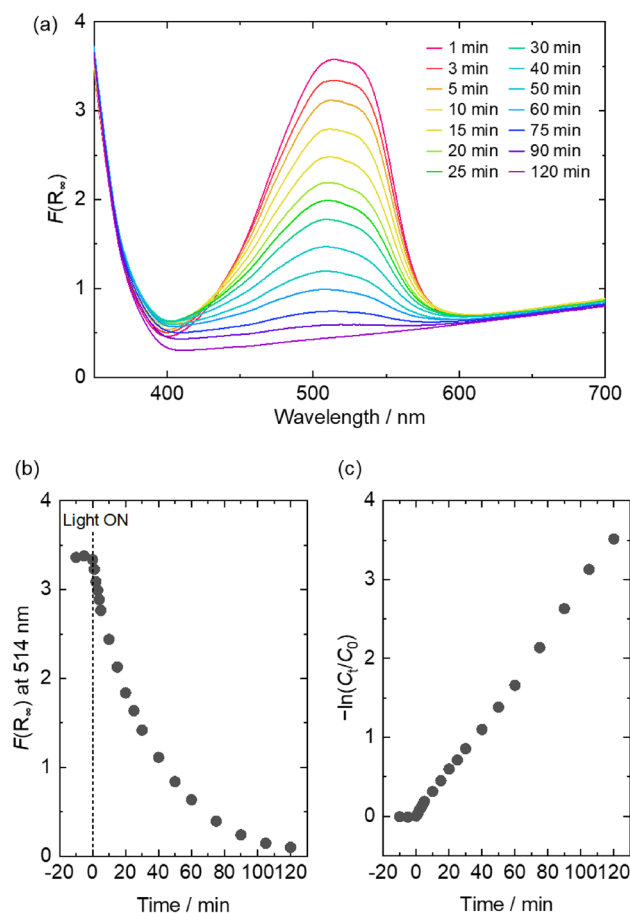


**Figure 6.** Decoloration of MO solution by using NTO-5-600 under VIS-light irradiation for appropriate time; (a) Kubelka–Munk plot, (b) time-dependent  $F(R_{\infty})$  decrease, and (c)  $-\ln(C_t/C_0)$  versus time plot.

anatase and rutile-based phase had gradient chemical composition of highly Nb doped  $\text{TiO}_2$  and poorly Nb doped  $\text{TiO}_2$ .

**Photocatalytic performance.** The photocatalytic performances of mechanochemically prepared powders were evaluated by decoloration of methyl orange (MO) aqueous solution, which is widely employed to investigate the properties of photocatalysts. In addition to NTO- $x$ - $y$ , pristine  $\text{TiO}_2$  and homogeneously Nb incorporated  $\text{TiO}_2$  synthesized by thermal plasma treatment<sup>32</sup> ( $\text{Nb}/(\text{Ti} + \text{Nb}) \sim 0.21$ , TP-20) were tested as a control. Diffuse reflectance measurements were employed to trace decoloration of MO. Figure 6 shows typical results of MO decoloration. The peaks correspond to MO were clearly decreased with light irradiation time (Fig. 6a,b). The calculated  $-\ln(C_t/C_0)$ , where  $C_0$  and  $C_t$  were MO concentrations of initial and  $t$  min light irradiated solutions, were plotted against irradiation time (Fig. 6c). According to the following Eq. (3) for first-order reaction, the rate constants were determined;

$$-\ln(C_t/C_0) = k \cdot t \quad (3)$$

where  $k$  and  $t$  were rate constants ( $k_{\text{UV}}$  and  $k_{\text{VIS}}$  under UV- and VIS-light irradiation, respectively) and irradiation time. Figure 7a,c are summary of  $k_{\text{UV}}$  and  $k_{\text{VIS}}$  for all the tested samples. Both of  $k_{\text{UV}}$  and  $k_{\text{VIS}}$  of NTO-0- $y$  were decreased with increasing heat treatment temperature same as  $\text{TiO}_2$ . In the case of  $\text{TiO}_2$  and NTO-0- $y$ , there was a relation between  $f_R$  and  $k_{\text{UV}}/k_{\text{VIS}}$ ; the photocatalytic activity decreased with increasing  $f_R$  (Fig. 7b,d). Decrease of  $k_{\text{UV}}$  is due to decrease of UV-light active anatase phase. The trend of  $k_{\text{VIS}}$  is different from reported studies, in which heat treated  $\text{TiO}_2$  photocatalysts showed volcanic plot of VIS-light activity against  $f_R$ <sup>50–52</sup>. The mechanism of photocatalytic activity in the case of anatase/rutile mixed phase was reported as follows; formation of heterojunction between anatase and rutile allows electrons transfer from rutile to anatase through interface that stabilizes charge separation and hinders charge recombination<sup>53</sup>. It is supposed that formed amorphous layers after mechanochemical treatment inhibit formation of anatase/rutile heterojunction, which disturbs electron transfer and results decrease of photocatalytic performance.

NTO-2-dry, NTO-5-dry, and NTO-10-dry showed significant increase of  $k_{\text{UV}}$  compared with NTO-0-dry and  $\text{TiO}_2$ . Although mechanochemically synthesized samples showed increased  $k_{\text{UV}}$  with increasing Nb doping amount, TP-20 having largest amount of Nb dopant revealed lowest  $k_{\text{UV}}$ . It is supposed that metastable doping by

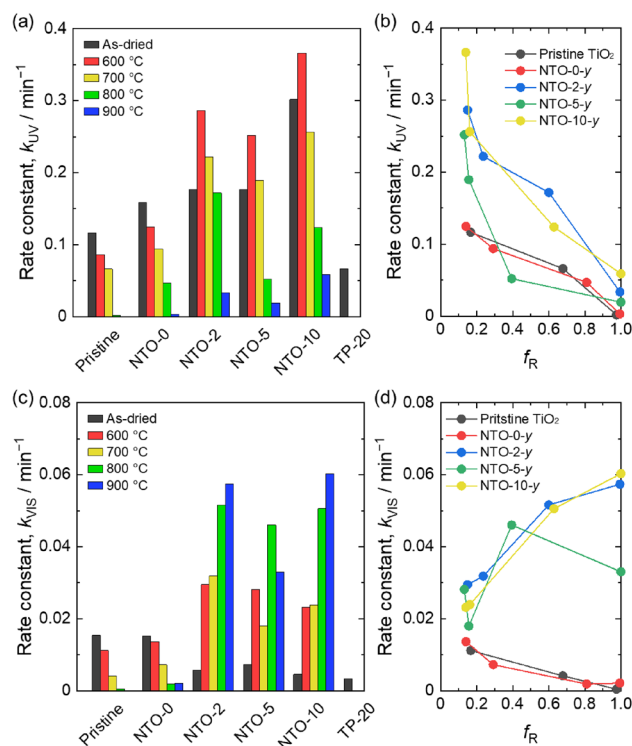


**Figure 7.** Rate constants,  $k_{UV}$  and  $k_{VIS}$ , of photocatalytic decoloration of MO under irradiation of (a) UV-light and (c) VIS-light of P25, NTO-0-y, NTO-0-y, NTO-5-y, NTO-10-y, and TP-20. The plots of  $f_R$  versus (b)  $k_{UV}$  and (d)  $k_{VIS}$  of P25, NTO-0-y, NTO-0-y, NTO-5-y, NTO-10-y, and TP-20 ( $600 \leq y \leq 900$ ).

mechanochemical treatment promoted photocatalytic performance. The  $k_{UV}$  further improved after heat treatment at 600 °C only in the case of mechanochemically Nb doped samples, which indicates formed chemical compositional gradient enhanced photocatalytic reaction. The  $k_{UV}$  tend to decrease with increasing heat treatment temperature above 600 °C, *i. e.*, increasing  $f_R$  as is shown in Fig. 7b. These results imply that Nb doped anatase nanoparticles having chemical compositional gradient structure are dominant component for an enhancement of UV-light photocatalytic performance. Although  $k_{VIS}$  of NTO-2-dry, NTO-5-dry, and NTO-10-dry were smaller than TiO<sub>2</sub> and NTO-0-dry, those were drastically increased after heat treatment. Considering  $k_{VIS}$  increased with further increasing  $f_R$ , it is supposed that Nb doped rutile nanoparticles gave significant enhancement of VIS-light photocatalytic performance. Surprisingly, NTO-2-800 showed significant high  $k_{UV}$  and  $k_{VIS}$  despite smaller specific surface area (3.21 m<sup>2</sup>/g) compared with pristine TiO<sub>2</sub> (45.7 m<sup>2</sup>/g), NTO-2-dry (53.6 m<sup>2</sup>/g) and TP-20 (87.2 m<sup>2</sup>/g). It is reported that Cu nanocluster-grafted Nb-doped TiO<sub>2</sub> showed VIS active photocatalytic performance owing to the energy level matching<sup>54</sup>. Considering these, formation of chemical compositional gradient structures will result energy level matching and lead excellent photocatalytic performance under both of UV- and VIS-light irradiation.

The effects of Nb doping on physical properties of TiO<sub>2</sub> have been reported; with increasing amount of Nb dopant, band gap energy became large and electron conductivity enhanced<sup>29,55–57</sup>. In addition, Nb doping leads generation of Ti<sup>3+</sup> improving photocatalytic activity<sup>58,59</sup>, which is not detected by XPS but detected by electron paramagnetic resonance technique<sup>60</sup>. Considering these reports, the hypothetic mechanism of mechanochemically prepared photocatalysts is summarized in Fig. 8. Electron–hole pair will generate at the poorly Nb doped TiO<sub>2</sub> (core part of nanoparticles) due to their smaller band gap energy compared with highly Nb doped TiO<sub>2</sub> (surface part of nanoparticles). Electrons will move to highly Nb doped TiO<sub>2</sub> because of larger conductivity. In addition, electron will transfer from rutile to trapping site of anatase around heterointerface, which is reported to be 0.8 eV lower than the conduction band edge of anatase<sup>61</sup>. These processes will stabilize charge separation and retard charge recombination. Considering Nernstian shift of conduction bands of TiO<sub>2</sub><sup>62,63</sup>, O<sub>2</sub><sup>•−</sup> radical formation through single-electron reduction reaction may be minor reaction. HO<sub>2</sub><sup>•</sup> radical and H<sub>2</sub>O<sub>2</sub> formed and attacked to MO molecules leading decoloration. The reported energy levels of valence band maximum and conduction band minimum of anatase, rutile, and TiNb<sub>2</sub>O<sub>7</sub> (as a typical example of Nb-rich titanium oxides) consistent with our hypothesis<sup>45,64</sup>.

## Conclusion

Nb doped TiO<sub>2</sub> were synthesized through mechanochemical reaction between TiO<sub>2</sub> (rutile/anatase) nanoparticles and TiNb<sub>2</sub>O<sub>7</sub> microparticles owing to the relatively lower elastic modulus of TiNb<sub>2</sub>O<sub>7</sub>. Homogeneously distributed Nb atoms tended to move to particle surface after high temperature heat treatment, which indicates initially

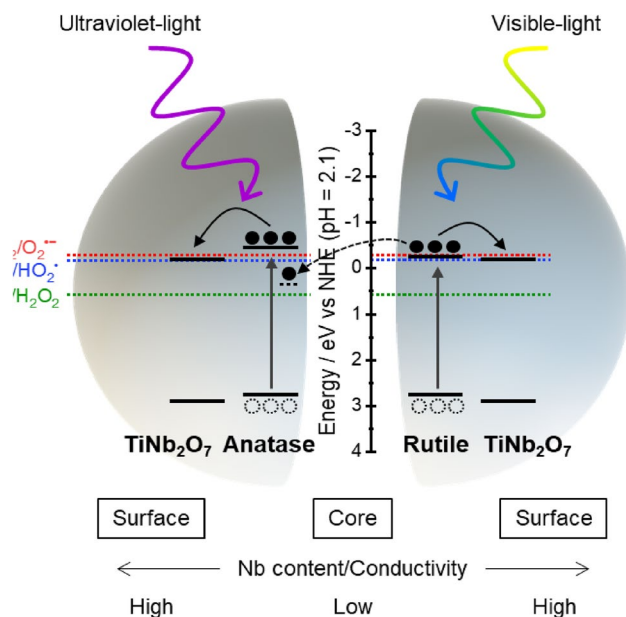


**Figure 8.** Schematic illustration of proposed mechanism of enhanced photocatalytic performance by Nb doped  $\text{TiO}_2$  nanoparticles with gradient chemical compositional structure. The reported energy levels were used<sup>145,61,64</sup>.

formed Nb doped  $\text{TiO}_2$  was metastable phase. Resultant materials had gradient chemical compositional structure of poorly Nb doped  $\text{TiO}_2$  core part and highly Nb doped  $\text{TiO}_2$  surface part. It was found that the materials with gradient chemical compositional heterojunction structure showed enhanced photocatalytic activity under both of UV- and VIS-light irradiation. Obtained results in this study indicate metastable materials prepared by mechanochemical treatment will show unique functions which are different from materials prepared by conventional thermal processes. It is expected to enhance not only photocatalytic property but also other functionalities, such as catalytic and electrochemical activity, by design materials through mechanochemical treatment.

Received: 10 May 2021; Accepted: 13 July 2021

Published online: 30 July 2021

## References

- Chen, X., Shen, S., Guo, L. & Mao, S. S. Semiconductor-based photocatalytic hydrogen generation. *Chem. Rev.* **110**, 6503–6570 (2010).
- Kumar, S. G. & Devi, L. G. Review on modified  $\text{TiO}_2$  photocatalysis under UV/visible light: Selected results and related mechanisms on interfacial charge carrier transfer dynamics. *J. Phys. Chem. A* **115**, 13211–13241 (2011).
- Wang, H. *et al.* Semiconductor heterojunction photocatalysts: Design, construction, and photocatalytic performances. *Chem. Soc. Rev.* **43**, 5234–5244 (2014).
- Miyauchi, M. *et al.* Visible-light-sensitive photocatalysts: Nanocluster-grafted titanium dioxide for indoor environmental remediation. *J. Phys. Chem. Lett.* **7**, 75–84 (2016).
- Li, Y., Hwang, D. S., Lee, N. H. & Kim, S. J. Synthesis and characterization of carbon-doped titania as an artificial solar light sensitive photocatalyst. *Chem. Phys. Lett.* **404**, 25–29 (2005).
- Hou, Y. D. *et al.* N-doped  $\text{SiO}_2/\text{TiO}_2$  mesoporous nanoparticles with enhanced photocatalytic activity under visible-light irradiation. *Chemosphere* **72**, 414–421 (2008).
- Perera, S. D. *et al.* Hydrothermal synthesis of graphene- $\text{TiO}_2$  nanotube composites with enhanced photocatalytic activity. *ACS Catal.* **2**, 949–956 (2012).
- Zhu, J., Zheng, W., He, B., Zhang, J. & Anpo, M. Characterization of Fe- $\text{TiO}_2$  photocatalysts synthesized by hydrothermal method and their photocatalytic reactivity for photodegradation of XRG dye diluted in water. *J. Mol. Catal. A Chem.* **216**, 35–43 (2004).
- Xiao, X. *et al.* One-pot solvothermal synthesis of three-dimensional (3D)  $\text{BiOI}/\text{BiOCl}$  composites with enhanced visible-light photocatalytic activities for the degradation of bisphenol-A. *J. Hazard. Mater.* **233–234**, 122–130 (2012).
- Huang, D. G., Liao, S. J., Liu, J. M., Dang, Z. & Petrik, L. Preparation of visible-light responsive N-F-codoped  $\text{TiO}_2$  photocatalyst by a sol-gel-solvothermal method. *J. Photochem. Photobiol. A Chem.* **184**, 282–288 (2006).
- Suda, Y., Kawasaki, H., Ueda, T. & Ohshima, T. Preparation of high quality nitrogen doped  $\text{TiO}_2$  thin film as a photocatalyst using a pulsed laser deposition method. *Thin Solid Films* **453–454**, 162–166 (2004).
- Sato, Y., Akizuki, H., Kamiyama, T. & Shigesato, Y. Transparent conductive Nb-doped  $\text{TiO}_2$  films deposited by direct-current magnetron sputtering using a  $\text{TiO}_{2-x}$  target. *Thin Solid Films* **516**, 5758–5762 (2008).
- James, S. L. *et al.* Mechanochemistry: Opportunities for new and cleaner synthesis. *Chem. Soc. Rev.* **41**, 413–447 (2012).
- Garay, A. L., Pichon, A. & James, S. L. Solvent-free synthesis of metal complexes. *Chem. Soc. Rev.* **36**, 846–855 (2007).
- Lea, M. C. Disruption of the silver haloid molecule by mechanical force. *Am. J. Sci.* **43**, 527–531 (1892).
- Leukel, S. *et al.* Mechanochemical access to defect-stabilized amorphous calcium carbonate. *Chem. Mater.* **30**, 6040–6052 (2018).
- Yamamoto, T. *et al.* Synthesis of the metastable cubic phase of  $\text{Li}_2\text{OHCl}$  by a mechanochemical method. *Inorg. Chem.* **59**, 11901–11904 (2020).
- Suryanarayana, C. & Al-Aqeeli, N. Mechanically alloyed nanocomposites. *Prog. Mater. Sci.* **58**, 383–502 (2013).

19. Prochowicz, D., Sasaki, M., Yadav, P., Grätzel, M. & Lewiński, J. Mechanoperovskites for photovoltaic applications: Preparation, characterization, and device fabrication. *Acc. Chem. Res.* <https://doi.org/10.1021/acs.accounts.9b00454> (2019).
20. MacHnicki, C. E., Fu, F., Jing, L., Chen, P. Y. & Wong, I. Y. Mechanochemical engineering of 2D materials for multiscale biointerfaces. *J. Mater. Chem. B* **7**, 6293–6309 (2019).
21. Palazon, F., El Ajjouri, Y. & Bolink, H. J. Making by grinding: Mechanochemistry boosts the development of halide perovskites and other multinary metal halides. *Adv. Energy Mater.* **1902499**, 1–13 (2019).
22. Rana, R. *et al.* Insights into the mechanism of the mechanochemical formation of metastable phases. *ACS Appl. Mater. Interfaces* **13**, 6785–6794 (2021).
23. Germann, L. S., Arhangelskis, M., Etter, M., Dinnebier, R. E. & Friščič, T. Challenging the Ostwald rule of stages in mechanochemical cocrystallisation. *Chem. Sci.* **11**, 10092–10100 (2020).
24. Fujishima, A. & Honda, K. Electrochemical photolysis of water at a semiconductor electrode. *Nature* **238**, 37–38 (1972).
25. Zhang, J., Wu, Y., Xing, M., Leghari, S. A. K. & Sajjad, S. Development of modified N doped TiO<sub>2</sub> photocatalyst with metals, nonmetals and metal oxides. *Energy Environ. Sci.* **3**, 715–726 (2010).
26. Marshall, R. Semiconductor composites: Strategies for enhancing charge carrier separation to improve photocatalytic activity. *Adv. Funct. Mater.* **24**, 2421–2440 (2014).
27. Jaiswal, R., Patel, N., Kothari, D. C. & Miotello, A. Improved visible light photocatalytic activity of TiO<sub>2</sub> co-doped with Vanadium and Nitrogen. *Appl. Catal. B Environ.* **126**, 47–54 (2012).
28. Murakami, M. *et al.* Anatase TiO<sub>2</sub> thin films grown on lattice-matched LaAlO<sub>3</sub> substrate by laser molecular-beam epitaxy. *Appl. Phys. Lett.* **78**, 2664–2666 (2001).
29. Furubayashi, Y. *et al.* A transparent metal: Nb-doped anatase TiO<sub>2</sub>. *Appl. Phys. Lett.* **86**, 1–3 (2005).
30. Tsuzuki, A., Murakami, H., Kani, K., Kawakami, S. & Torii, Y. Preparation of Nb-doped TiO<sub>2</sub> films by the sol-gel method. *J. Mater. Sci. Lett.* **9**, 624–626 (1990).
31. Ruiz, A. M., Dezanneau, G., Arbiol, J., Cornet, A. & Morante, J. R. Insights into the structural and chemical modifications of Nb additive on TiO<sub>2</sub> nanoparticles. *Chem. Mater.* **16**, 862–871 (2004).
32. Zhang, C. *et al.* High-concentration niobium (V) doping into TiO<sub>2</sub> nanoparticles synthesized by thermal plasma processing. *J. Mater. Res.* **26**, 658–671 (2011).
33. Saito, K., Yi, E., Laine, R. M. & Sugahara, Y. Preparation of Nb-doped TiO<sub>2</sub> nanopowder by liquid-feed spray pyrolysis followed by ammonia annealing for tunable visible-light absorption and inhibition of photocatalytic activity. *Ceram. Int.* **46**, 1314–1322 (2020).
34. Ohsaka, T., Izumi, F. & Fujiki, Y. Raman spectrum of anatase, TiO<sub>2</sub>. *J. Raman Spectrosc.* **7**, 321–324 (1978).
35. Chen, X., Liu, L., Yu, P. Y. & Mao, S. S. Increasing solar absorption for photocatalysis with black hydrogenated titanium dioxide nanocrystals. *Science* **331**, 746–750 (2011).
36. Wachtman, J. B., Tefft, W. E. & Lam, D. G. Elastic constants of rutile (TiO<sub>2</sub>). *J. Res. Natl. Bur. Stand. Sect. A Phys. Chem.* **66A**, 465 (1962).
37. Perfler, L. *et al.* Nanoindentation, high-temperature behavior, and crystallographic/spectroscopic characterization of the high-refractive-index materials TiTa<sub>2</sub>O<sub>7</sub> and TiNb<sub>2</sub>O<sub>7</sub>. *Inorg. Chem.* **54**, 6836–6848 (2015).
38. Santara, B., Giri, P. K., Imakita, K. & Fujii, M. Microscopic origin of lattice contraction and expansion in undoped rutile TiO<sub>2</sub> nanostructures. *J. Phys. D Appl. Phys.* **47**, 215302 (2014).
39. Kamisaka, H., Hitosugi, T., Suenaga, T., Hasegawa, T. & Yamashita, K. Density functional theory based first-principle calculation of Nb-doped anatase TiO<sub>2</sub> and its interactions with oxygen vacancies and interstitial oxygen. *J. Chem. Phys.* **131**, 034702 (2009).
40. Lee, H.-Y. & Robertson, J. Doping and compensation in Nb-doped anatase and rutile TiO<sub>2</sub>. *J. Appl. Phys.* **113**, 213706 (2013).
41. Spurr, R. A. & Myers, H. Quantitative analysis of anatase-rutile mixtures with an X-ray diffractometer. *Anal. Chem.* **29**, 760–762 (1957).
42. Begin-colin, S., Caer, G. L., Mocellin, A. & Zandona, M. Polymorphic transformations of titania induced by ball milling. *Philos. Mag. Lett.* **69**, 1–7 (1994).
43. Sayers, C. N. & Armstrong, N. R. X-ray photoelectron spectroscopy of TiO<sub>2</sub> and other titanate electrodes and various standard Titanium oxide materials: Surface compositional changes of the TiO<sub>2</sub> electrode during photoelectrolysis. *Surf. Sci.* **77**, 301–320 (1978).
44. Darlinski, A. Angle resolved XPS studies of oxides at Nb-, NbN-, NbC- and Nb<sub>3</sub>Sn- surfaces. *IEEE Trans. Magn.* **23**, 1381–1384 (1987).
45. Yu, Z. *et al.* Dual modification of TiNb<sub>2</sub>O<sub>7</sub> with nitrogen dopants and oxygen vacancies for selective aerobic oxidation of benzylamine to imine under green light. *J. Mater. Chem. A* **5**, 4607–4615 (2017).
46. Yao, Z. *et al.* Superior high-rate lithium-ion storage on Ti<sub>2</sub>Nb<sub>10</sub>O<sub>29</sub> arrays via synergistic TiC/C skeleton and N-doped carbon shell. *Nano Energy* **54**, 304–312 (2018).
47. Sun, R. *et al.* High rate capability performance of ordered mesoporous TiNb<sub>6</sub>O<sub>17</sub> microsphere anodes for lithium ion batteries. *Dalt. Trans.* **46**, 17061–17066 (2017).
48. Li, S., Chen, J., Gong, X., Wang, J. & Lee, P. S. Holey graphene-wrapped porous TiNb<sub>24</sub>O<sub>62</sub> microparticles as high-performance intercalation pseudocapacitive anode materials for lithium-ion capacitors. *NPG Asia Mater.* **10**, 406–416 (2018).
49. Cardona, M. & Harbeke, G. Optical properties and band structure of wurtzite-type crystals and rutile. *Phys. Rev.* **137**, A1467–A1476 (1965).
50. Su, R. *et al.* How the anatase-to-rutile ratio influences the photoreactivity of TiO<sub>2</sub>. *J. Phys. Chem. C* **115**, 24287–24292 (2011).
51. Nair, R. G., Paul, S. & Samdarshi, S. K. High UV/visible light activity of mixed phase titania: A generic mechanism. *Sol. Energy Mater. Sol. Cells* **95**, 1901–1907 (2011).
52. Ishigaki, T. *et al.* Enhanced visible-light photocatalytic activity of anatase-rutile mixed-phase nano-size powder given by high-temperature heat treatment. *R. Soc. Open Sci.* **7**, 191539 (2020).
53. Hurum, D. C. *et al.* Probing reaction mechanisms in mixed phase TiO<sub>2</sub> by EPR. *J. Electron Spectros. Relat. Phenomena* **150**, 155–163 (2006).
54. Liu, M., Qiu, X., Hashimoto, K. & Miyauchi, M. Cu(ii) nanocluster-grafted, Nb-doped TiO<sub>2</sub> as an efficient visible-light-sensitive photocatalyst based on energy-level matching between surface and bulk states. *J. Mater. Chem. A* **2**, 13571–13579 (2014).
55. Kurita, D., Ohta, S., Sugiura, K., Ohta, H. & Koumoto, K. Carrier generation and transport properties of heavily Nb-doped anatase TiO<sub>2</sub> epitaxial films at high temperatures. *J. Appl. Phys.* **100**, 1–4 (2006).
56. Zhang, S. X. *et al.* Niobium doped TiO<sub>2</sub>: Intrinsic transparent metallic anatase versus highly resistive rutile phase. *J. Appl. Phys.* **102**, 1–5 (2007).
57. Wolfenstine, J. & Allen, J. L. Electrical conductivity and charge compensation in Ta doped Li<sub>4</sub>Ti<sub>5</sub>O<sub>12</sub>. *J. Power Sources* **180**, 582–585 (2008).
58. Kiwi, J., Suss, J. T. & Szapiro, S. EPR spectra of niobium-doped TiO<sub>2</sub> and implications for water photocleavage processes. *Chem. Phys. Lett.* **106**, 135–138 (1984).
59. Valigi, M. *et al.* A structural, thermogravimetric, magnetic, electron spin resonance, and optical reflectance study of the NbO<sub>x</sub>TiO<sub>2</sub> system. *J. Solid State Chem.* **77**, 255–263 (1988).
60. Biedrzycki, J., Livraghi, S., Giamello, E., Agnoli, S. & Granozzi, G. Fluorine- and niobium-doped TiO<sub>2</sub>: Chemical and spectroscopic properties of polycrystalline n-type-doped anatase. *J. Phys. Chem. C* **118**, 8462–8473 (2014).

61. Leytner, S. & Hupp, J. T. Evaluation of the energetics of electron trap states at the nanocrystalline titanium dioxide/aqueous solution interface via time-resolved photoacoustic spectroscopy. *Chem. Phys. Lett.* **330**, 231–236 (2000).
62. O'Regan, B., Graetzel, M. & Fitzmaurice, D. Optical electrochemistry. 2. Real-time spectroscopy of conduction band electrons in a metal oxide semiconductor electrode. *J. Phys. Chem.* **95**, 10525–10528 (1991).
63. Kavan, L., Grätzel, M., Gilbert, S. E., Klemenz, C. & Scheel, H. J. Electrochemical and photoelectrochemical investigation of single-crystal anatase. *J. Am. Chem. Soc.* **118**, 6716–6723 (1996).
64. Park, K. W. & Kolpak, A. M. Optimal methodology for explicit solvation prediction of band edges of transition metal oxide photocatalysts. *Commun. Chem.* **2**, 1–10 (2019).

## Acknowledgements

The present work is partially supported by JSPS KAKENHI Grant Number JP20K15368, JSPS Core-to-Core Program, Foundation for the Promotion of Ion Engineering, Izumi Science and Technology Foundation (2019-J-112), International Network on Polyoxometalate Science at Hiroshima University, Leading Initiative for Excellent Young Researchers from the Ministry of Education, Culture Sports, Science and Technology (MEXT) of Japan, and the Strategic Research Foundation at Private Universities from MEXT of Japan. We thank Aya Ohkubo for grateful help for XPS measurements.

## Author contributions

Study design: N.T., T.U., T.I. Experimental analyses: N.T., R.K. Data evaluation: N.T., R.K., T.I. All authors read and approved the final version. N.T. and T.I. are corresponding authors because they gave equal contribution.

## Competing interests

The authors declare no competing interests.

## Additional information

**Supplementary Information** The online version contains supplementary material available at <https://doi.org/10.1038/s41598-021-94512-x>.

**Correspondence** and requests for materials should be addressed to N.T. or T.I.

**Reprints and permissions information** is available at [www.nature.com/reprints](http://www.nature.com/reprints).

**Publisher's note** Springer Nature remains neutral with regard to jurisdictional claims in published maps and institutional affiliations.



**Open Access** This article is licensed under a Creative Commons Attribution 4.0 International License, which permits use, sharing, adaptation, distribution and reproduction in any medium or format, as long as you give appropriate credit to the original author(s) and the source, provide a link to the Creative Commons licence, and indicate if changes were made. The images or other third party material in this article are included in the article's Creative Commons licence, unless indicated otherwise in a credit line to the material. If material is not included in the article's Creative Commons licence and your intended use is not permitted by statutory regulation or exceeds the permitted use, you will need to obtain permission directly from the copyright holder. To view a copy of this licence, visit <http://creativecommons.org/licenses/by/4.0/>.

© The Author(s) 2021